# Results of Flexible Spacecraft Attitude Control Studies Utilizing Hybrid Coordinates

PETER W. LIKINS*
*University of California, Los Angeles, Calif.*
AND
GERALD E. FLEISCHER†
*Jet Propulsion Laboratory, Pasadena, Calif.*

**Explicit analyses are presented in sufficient detail to establish the utility in flexible space vehicle control system design of a hybrid coordinate formulation, employing a combination of discrete and distributed (modal) coordinates. A three-stage process for the design of attitude control systems for flexible vehicles is described: 1) preliminary design is based on root locus plots for single-axis response of linearized systems with sharply truncated modal coordinate matrices; 2) modifications are imposed as required by eigenvalue analyses of coupled linear systems; and 3) design confirmation is established by complex, nonlinear differential equation simulation using digital computer numerical integration. These procedures are illustrated by application to two vehicle models. A very simple model is used to demonstrate the potentially destabilizing influence of vehicle flexibility, and corresponding results are shown for a realistically complex model of the Thermoelectric Outer Planet Spacecraft (TOPS).**

## Nomenclature

$\bar{A}$ = $\bar{\phi}^T(M/\mathfrak{M})\Sigma_{E0}$
$\hat{\mathbf{b}}_1,\hat{\mathbf{b}}_2,\hat{\mathbf{b}}_3$ = unit vectors directed along body-fixed principal axis
$d$ = 3 × 1 matrix of measure numbers of vector from vehicle mass center to motor gimbal point
$d^0$ = 3 × 1 matrix of nominal $d$ value
$\bar{D}$ = $(s^2E + 2s\bar{\zeta}\bar{\sigma} + \bar{\sigma}^2)^{-1}$
$E$ = 3 × 3 identity matrix
$E^1$ = $[100]^T$, matrix operator
$E^2$ = $[010]^T$, matrix operator
$E^3$ = $[001]^T$, matrix operator
$F$ = 3 × 1 matrix of external force measure numbers $F_1,F_2,F_3$
$F_0$ = magnitude of constant thrust from the motor
$G(s)$ = vehicle dynamics matrix transfer function
$h$ = 3 × 1 matrix of internal angular momentum measure numbers due to rotors
$h_0$ = 3 × 1 matrix of angular momentum measure numbers of a constant speed rotor
$H(s)$ = feedback control block matrix transfer function
$I$ = 3 × 3 inertia matrix of the undeformed vehicle, for the mass center
$K$ = system open loop Bode gain
$K'$ = feedback controller Bode gain
$M$ = $6n \times 6n$ matrix of masses and inertias of appendage subbodies
$\mathfrak{M}$ = total vehicle mass
$n$ = number of rigid bodies in discrete model of the appendage
$N$ = number of appendage modal coordinates retained after truncation
$O$ = point fixed in base body at nominal vehicle mass center
$p,z$ = poles and zeros of the system characteristic equation
$Q$ = label of a reference point fixed at the interface between rigid body and appendage
$r^i$ = 3 × 1 matrix of measure numbers of the vector from $Q$ to mass center of the $i$th body of the undeformed appendage
$R$ = 3 × 1 matrix of measure numbers $R_1$, $R_2$, $R_3$ of a vector from point $O$
$\mathfrak{R}_\alpha{}^j$ = normalized reduced inertia for axis $\alpha$ and mode $j$
$s$ = Laplace operator
$T$ = 3 × 1 matrix of external torque measure numbers $T_1,T_2,T_3$ referred to vehicle mass center
$T^R$ = 3 × 1 matrix of reference torque measure numbers
$\gamma_2,\gamma_3$ = motor gimbal angles
$\bar{\delta}$ = $-\bar{\phi}^TM(\Sigma_{0E} - \Sigma_{E0}\tilde{R} - r\Sigma_{E0})$
$\bar{\zeta}$ = $N \times N$ diagonal truncated matrix of damping ratios $\zeta_1, \ldots, \zeta_N$ in the $N$ modes of appendage vibration
$\zeta_G$ = gyro dynamics damping ratio
$\zeta_s$ = gimbal servo actuator dynamics damping ratio
$\bar{\eta}$ = $N \times 1$ truncated matrix of modal coordinates $\eta_1, \ldots, \eta_N$ of the appendage
$\theta$ = 3 × 1 matrix of 1-2-3 attitude angles $\theta_1,\theta_2,\theta_3$ of the rigid body
$\bar{\sigma}$ = $N \times N$ truncated matrix of natural frequencies $\sigma_1, \ldots, \sigma_N$
$\Sigma_{E0}$ ≡ $[E0E0 \ldots E0]^T$, a $6n \times 3$ matrix operator
$\Sigma_{0E}$ ≡ $[0E0E \ldots 0E]^T$, a $6n \times 3$ matrix operator
$\tau_G$ = gyro rate-to-position gain
$\tau_F$ = autopilot time constant
$\tau_p$ = autopilot path guidance time constant
$\bar{\phi}$ = $6n \times N$ truncated matrix whose columns are eigenvectors of the appendage
$\omega_G$ = gyro natural frequency
$\omega_S$ = gimbal servo actuator natural frequency
0 = nullity, as a scalar or 3 × 3 matrix

### *Subscripts*

$j$ = $j$th modal coordinate
0 = scalar magnitude of a vector
$x,y$ = pitch and yaw axes, respectively, of the TOPS vehicle
$\alpha$ = any one of the vehicle principal axes
1,2,3 = vehicle principal axes

### *Superscripts*

$i$ = $i$th subbody of the appendage
$j$ = $j$th modal coordinate
0 = nominal column matrix
$T$ = denotes matrix transposition

Presented as Paper 70-20 at AIAA 8th Aerospace Sciences Meeting, New York, January 19–21, 1970; submitted May 6, 1970; revision received November 4, 1970. This paper presents the results of one phase of research carried out at the Jet Propulsion Laboratory, California Institute of Technology, under Contract NAS 7-100, sponsored by NASA.

* Associate Professor; also Consultant to the Jet Propulsion Laboratory.
† Senior Engineer.

## Introduction

INTERACTION between spacecraft attitude control systems and flexible structures is receiving increasing attention,[1-5] because many appendages cannot reasonably be designed with sufficient rigidity to justify the traditional assumption that the dynamic response to attitude control devices can be uncoupled from vehicle vibrations, and when coupling is present the result may be control system instability. It has therefore become necessary to confront directly the coupled equations of vibration and attitude control. Analytical techniques developed for aircraft and missile applications employ coordinates representing the normal modes of (small) deformation of the vehicle. This "vehicle normal coordinate" approach has been successfully applied to space vehicles of a limited class,[3] but for many modern spacecraft this method is inappropriate. Specifically, if the vehicle includes any rotating parts, discrete dampers, or nonlinearities, the traditional vehicle normal coordinate approach is generally inadequate. Various dynamical formalisms have been proposed for the direct simulation of a system of interconnected and actively controlled rigid bodies,[6-9] but this "discrete coordinate" approach sacrifices the advantages afforded by distributed or modal coordinates when structural deformations can be assumed to remain small.

The "hybrid coordinate" method[10] combines certain of the advantages of discrete and distributed (modal) coordinates by using both simultaneously. In the present paper, previous theoretical development[1] is extended as necessary for applications of practical interest, and the results of detailed studies of two vehicles are illustrated. A three-stage procedure is devised for the systematic design of control systems for flexible vehicles, progressing from single-axis root locus studies through eigenvalue analyses to nonlinear digital similations.

## Procedures

In Refs. 1 and 10, the hybrid coordinate method is developed for the mathematical simulation of the motions of a class of assemblages of rigid bodies and flexible appendages. In final form the discrete coordinates of most (but not all) of the particles and rigid bodies in the system are replaced by distributed (or *modal*) coordinates. An essential step in the derivation process is the isolation of a subset of the original total system of discrete variable differential equations, such that the homogeneous forms of the isolated equations are linear, constant-coefficient equations in the corresponding subset of the system variables. In physical terms, this form of the equations occurs when a space vehicle is modeled as a collection of rigid bodies whose angular velocities deviate only slightly from known constants, with attached elastic appendages that undergo small deformations. Coordinate transformations of those system variables in the linear subset of equations then produce distributed coordinates describing the modal response of the elastic appendages of the vehicle, while the attitude coordinates of the rigid bodies of the system remain discrete. The modal coordinate matrix for the appendages is then truncated for efficiency in simulation. This technique provides equations of motion applicable to a wide variety of space vehicles,[10] but published applications limited to dual-spin spacecraft[11] do not reveal the potentially destabilizing influence of flexibility on control system performance.

As a special case of the matrix equations of motion applicable to a vehicle idealized as a rigid body with a rigid rotor and a flexible appendage, and therefore not amenable to analysis by the vehicle normal coordinate method, consider the following (from Ref. 10, Eq. 216 and 224, after deleting external forces on the appendage and eliminating the linear oscillator):

$$T = I\ddot{\theta} - \tilde{h}\dot{\theta} - \tilde{\delta}^T\ddot{\eta} + \dot{h} \tag{1}$$

$$\ddot{\eta} + 2\tilde{\zeta}\tilde{\sigma}\dot{\eta} + \tilde{\sigma}^2\eta = \delta\ddot{\theta} - \tilde{\phi}^T M\Sigma_{E0}F/\mathfrak{M} \tag{2}$$

where

$$\tilde{\delta} = -\tilde{\phi}^T M(\Sigma_{0E} - \Sigma_{E0}\tilde{R} - \tilde{r}\Sigma_{E0})$$

and (for unit consistency) Eq. (2) has been multiplied by an identity matrix with units the reciprocal of inertia units. Here the vehicle is idealized as rigid body with a system of body-fixed rigid symmetric rotors and a flexible appendage.

In these equations all matrices are expressed in the same body-fixed vector basis

$$\tilde{h} \equiv \begin{bmatrix} 0 & -h_3 & h_2 \\ h_3 & 0 & -h_1 \\ -h_2 & h_1 & 0 \end{bmatrix} \tag{3}$$

and

$$\tilde{R} \equiv \begin{bmatrix} 0 & -R_3 & R_2 \\ R_3 & 0 & -R_1 \\ -R_2 & R_1 & 0 \end{bmatrix} \tag{4}$$

$\tilde{r}$ is a $6n \times 6n$ matrix

$$\tilde{r} = \begin{bmatrix} \tilde{r}^1 & & & & & 0 \\ & 0 & & & & \\ & & \tilde{r}^2 & & & \\ & & & 0 & & \\ & & & & \ddots & \\ & & & & & \tilde{r}^n \\ 0 & & & & & 0 \end{bmatrix} \tag{5}$$

wherein each $\tilde{r}^i$ is a matrix of the same form as Eqs. (3) and (4). Overdot denotes time differentiation. The general significance of the tilde ($\sim$) operator on a $3 \times 1$ matrix is evident from Eqs. (3) and (4).

In most spacecraft attitude control problems, $T$ in Eq. (1) becomes the primary differentiated variable in an additional differential equation whose character is established by a control law. The external force $F$ is usually zero, unless the attitude control is accomplished by an autopilot for a midcourse motor, in which case a control law on the direction of $F$ provides a differential equation to augment Eqs. (1) and (2). The internal angular momentum $h$ may also be established by a control law (as with a reaction wheel control system or a dual-spin system). The immediate objective here is to establish a procedure for the practical utilization of Eqs. (1) and (2). Their most straightforward application is in combination with one of the suggested control equations in a numerical integration program. If the control equations are highly nonlinear, this may be the only way to use Eqs. (1) and (2), but in many problems of interest useful preliminary approximations can be obtained with linearized control equations. When this is possible, it becomes computationally inefficient to rely upon numerical integration to examine each of the many variations emerging in the design process, and numerical determination of eigenvalues from the linearized state equation is often an efficient alternative. It should be noted that the truncation of the $6n \times 1$ modal coordinate matrix $\eta$ to form the $N \times 1$ matrix $\bar{\eta}$ is a somewhat subjective process, and some investigation of the influence of various higher frequency appendage modes on the rigid-body attitude matrix $\theta$ may be necessary. Since high-frequency response is costly in terms of time and accuracy in numerical integration, the eigenvalue program may accomplish this investigation most efficiently.

Among the features of the hybrid coordinate approach is the explicit retention of $\theta_1$, $\theta_2$, $\theta_3$ in the equations. In many applications, the interest of the attitude-control engineer is

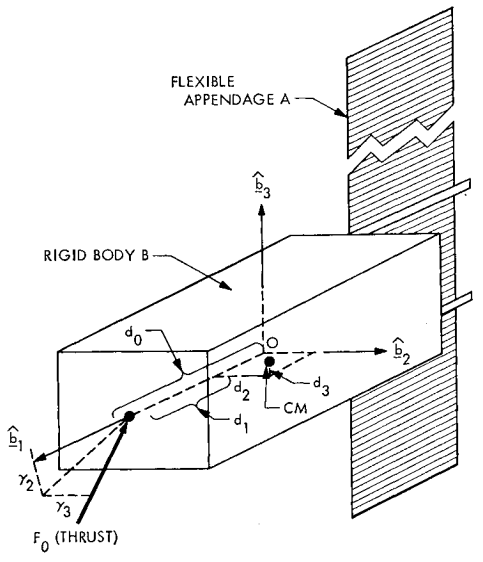


**Fig. 1 Coordinates for autopilot control.**

sharply focused on these variables, and he is unconcerned about the appendage deformations represented by $\bar{\eta}$. He may eliminate $\bar{\eta}$ from consideration by making a Laplace transformation, provided that $h$ is approximately a constant, say $h_0$. Equations (1) and (2), become

$$T(s) = s^2 I\theta(s) - s\tilde{h}_0\theta(s) - s^2\bar{\delta}^T\bar{\eta}(s) + sh(s) \tag{6}$$

and

$$s^2\bar{\eta}(s) + 2s\bar{\zeta}\bar{\sigma}\bar{\eta}(s) + \bar{\sigma}^2\bar{\eta}(s) = s^2\bar{\delta}\theta(s) - \bar{\phi}^T M\Sigma_{E0}F(s)/\mathfrak{M} \tag{7}$$

Solving Eq. (7) for $\bar{\eta}(s)$ and substituting into Eq. (6), we obtain

$$T(s) - sh(s) - s^2\bar{\delta}^T\bar{D}\bar{\phi}^T M\Sigma_{E0}F(s)/\mathfrak{M} = (s^2 I - s\tilde{h}_0 - s^4\bar{\delta}^T\bar{D}\bar{\delta})\theta(s) \tag{8}$$

where $\bar{D} \equiv (s^2 E + 2s\bar{\zeta}\bar{\sigma} + \bar{\sigma}^2)^{-1}$. Equation (8) can provide a variety of useful transfer functions, depending on the basic control system actuation chosen. If, for example, $F$ and $h$ are essentially zero, the matrix transfer function is available directly from

$$T(s) = (s^2 I - s^4\bar{\delta}^T\bar{D}\bar{\delta})\theta(s) \tag{9}$$

This result would for example apply to a three-axis reaction-jet control system with resultant $F = 0$.

The introduction of a constant-speed rotor merely changes Eq. (9) by adding the term $-s\tilde{h}_0\theta(s)$ on the right side. The resulting transfer function would describe a dual-spin spacecraft under body-fixed reaction-jet control for reorientation.

If the sole control comes from reaction wheels, so that $T$ and $F$ in Eq. (8) are zero, nonlinearities in system variables occur unless $h$ may be linearized about some constant value $h_0$. When this is an acceptable approximation, an appropriate transfer function is available in Eq. (8), with $T \equiv F \equiv 0$.

It should be noted that $\tilde{h}$ in Eq. (1) is formally restricted in a way that includes axisymmetric reaction wheels or momentum wheels with body-fixed axes, but apparently excludes control moment gyros (CMG's). The only change formally required to accommodate CMG's, however, is in the recognition that the vehicle inertia matrix $I$ varies with CMG gimbal rotation, and this variation is usually of no engineering significance. A more serious obstacle arises when one seeks a transfer function for the CMG system, since the use of $\tilde{h}_0$ as in Eq. (8) may be precluded by large and rapid changes in the gimbal angles.

As a final example, consider the autopilot transfer function for a rotorless vehicle ($h = 0$) under thrust of constant magnitude $F_0$ and variable direction. To focus ideas, assume that nominally the thrust vector is directed along the principal axis parallel to $\hat{\mathbf{b}}_1$ and passing through the body-fixed point $O$ which is the mass center of the vehicle when undeformed. (See Fig. 1). The thrust direction is varied by the small gimbal angle rotations $\gamma_2(t)$ and $\gamma_3(t)$ about axes parallel to $\hat{\mathbf{b}}_2$ and $\hat{\mathbf{b}}_3$, respectively. The vector $\mathbf{d}$ locates from the mass center c.m. the gimbal point at which the thrust vector is applied. When the vehicle appendage is undeformed, the measure numbers of $\mathbf{d}$ have the values $d_1 = d_0$, $d_2 = d_3 = 0$, so changes in this vector due to small deformations remain small. (Thrust direction control is accomplished with jet vanes or motor gimbal of negligible mass.) If $d^0$ is the column matrix representing the nominal value of $\mathbf{d}$, and the notation of Refs. 1 and 10 is adopted to describe the mass center shift from $O$ to c.m. due to appendage deformations, the matrix $d$ which represents $\mathbf{d}$ becomes

$$d = d^0 - \Sigma_{E0}{}^T(M/\mathfrak{M})\bar{\phi}\bar{\eta} \tag{10}$$

With the definitions

$$F^0 \equiv \begin{bmatrix} -F_0 \\ 0 \\ 0 \end{bmatrix} \qquad \gamma \equiv \begin{bmatrix} 0 \\ \gamma_2 \\ \gamma_3 \end{bmatrix} \tag{11}$$

the engine force under a general (but small angle) gimbal rotation is given by

$$F = F^0 - \tilde{F}^0\gamma = \begin{bmatrix} -F_0 \\ -F_0\gamma_3 \\ F_0\gamma_2 \end{bmatrix} \tag{12}$$

[See Eqs. (3) and (4) for the meaning of the tilde operator.] Thus the moment applied about the spacecraft mass center becomes $\mathbf{d} \times \mathbf{F}$, or in matrix terms

$$T = \tilde{d}F = \begin{bmatrix} d_2F_3 - d_3F_2 \\ d_3F_1 - d_1F_3 \\ d_1F_2 - d_2F_1 \end{bmatrix} \tag{13}$$

With Eq. (12), this moment becomes (in the linearized approximation)

$$T = \tilde{d}F^0 - \tilde{d}^0\tilde{F}^0\gamma = -\tilde{F}^0 d - \tilde{d}^0\tilde{F}^0\gamma \tag{14}$$

or, since $\tilde{F}^0 d^0 = 0$,

$$T = \tilde{F}^0\Sigma_{E0}{}^T(M/\mathfrak{M})\bar{\phi}\bar{\eta} - \tilde{d}^0\tilde{F}^0\gamma \tag{15}$$

The scalar elements in $T$ can be obtained when necessary by combining the preceding equations to obtain

$$T_1 = 0 \tag{16}$$

$$T_2 = E^{3T}\Sigma_{E0}{}^T(M/\mathfrak{M})\bar{\phi}\bar{\eta}F_0 - d_0F_0\gamma_2 \tag{17}$$

$$T_3 = E^{2T}\Sigma_{E0}{}^T(M/\mathfrak{M})\bar{\phi}\bar{\eta}F_0 - d_0F_0\gamma_3 \tag{18}$$

Substitution into Eq. (8) of the special case defined by Eqs. (12) and (15) with $h \equiv 0$, and use of Eq. (7) to replace $\bar{\eta}(s)$ by the appropriate function of $\gamma(s)$ and $\theta(s)$, namely

$$\bar{\eta}(s) = \bar{D}\{s^2\bar{\delta}\theta(s) - \bar{\phi}^T(M/\mathfrak{M})\Sigma_{E0}[F^0 + \tilde{F}^0\gamma(s)]\} \tag{19}$$

yields

$$-s^2\bar{\delta}^T\bar{D}\bar{A}F^0 - \tilde{F}^0\bar{A}^T\bar{D}\bar{A}F^0 + (-\tilde{d}^0\tilde{F}^0 - s^2\bar{\delta}^T\bar{D}\bar{A}\tilde{F}^0 - \tilde{F}^0\bar{A}^T\bar{D}\bar{A}\tilde{F}^0)\gamma(s) = (s^2 I - s^4\bar{\delta}^T\bar{D}\bar{\delta} - s^2\tilde{F}^0\bar{A}^T\bar{D}\bar{\delta})\theta(s) \tag{20}$$

where $\bar{A} = \bar{\phi}^T(M/\mathfrak{M})\Sigma_{E0}$. The first two terms in Eq. (20) involve neither $\gamma(s)$ nor $\theta(s)$, so they may appear to jeopardize the transfer function concept. These terms represent the influence on $\theta$ of the constant thrust $F_0$ in the nominal direction (with $\gamma_2 = \gamma_3 = 0$). This thrust imparts some deformation to the appendage, which in turn may introduce an attitude error $\theta$. Since this is a steady-state deformation, unchanging for constant thrust magnitude $F_0$, the resulting $\theta$ is not of primary interest here, and will be ignored. In most applica-

tions of interest, the first term in the braces multiplying $\gamma(s)$ and the first two terms in the braces multiplying $\theta(s)$ are dominant. Then Eq. (20) is fully equivalent to Eq. (9).

Equations (9) and (20) represent special cases of Eq. (8), and from each of these a matrix transfer function of practical utility can be obtained. In many cases of interest, the matrix transfer function is dominated by its diagonal terms, and scalar transfer functions for single-axis response can be extracted. The generation of root-locus plots then becomes a simple matter, easily automated. Equation (9) is directly applicable for three-axis gas jet control, and it provides a useful approximation for midcourse motor autopilot control and reaction wheel control (ignoring stored momentum). This simple transfer function is therefore selected for further study.

The matrix $\bar{D}$ in Eq. (9) is diagonal with elements typified by $(s^2 + 2\zeta_j\sigma_j s + \sigma_j^2)^{-1}$. The principle of superposition applies to this linear system, so the matrix transfer function of Eq. (9) can as well be written

$$\theta(s) = \left[ Is^2 - s^4 \sum_{j=1}^{N} \frac{\delta^{jT}\delta^j}{(s^2 + 2\zeta_j\sigma_j s + \sigma_j^2)} \right]^{-1} T(s) \quad (21)$$

In the block diagram in Fig. 2, the open-loop transfer function $G(s)$ associated with the dynamics block alone is available directly from Eq. (21), while the control system matrix transfer function is given by

$$\theta(s) = [G^{-1}(s) + H(s)]^{-1}T^R(s) \quad (22)$$

in the notation of Fig. 2.

When the matrix transfer function is diagonal, representation of the vehicle response in terms of three scalar transfer functions becomes possible. The scalar open-loop transfer function $G_\alpha(s)$ for axis $\alpha(\alpha = 1, 2, 3)$ is then available from Eq. (21) as $G_\alpha(s) \equiv \theta_\alpha(s)/T_\alpha(s)$, and if only mode $j$ is retained in truncation, this transfer function becomes

$$G_\alpha(s) = \frac{s^2 + 2\zeta_j\sigma_j s + \sigma_j^2}{I_\alpha s^2 [s^2(1 - \delta_\alpha{}^j\delta_\alpha{}^j/I_\alpha) + 2\zeta_j\sigma_j s + \sigma_j^2]} \quad (23)$$

The quantity in parentheses is called the "normalized reduced inertia" for axis $\alpha$ and mode $j$, and given the symbol $\mathfrak{R}_\alpha{}^j$, or simply $\mathfrak{R}$ if the identifying subscript and superscript are clear from the context. This label implies a physical significance for the scalar quantity $\delta_\alpha{}^j\delta_\alpha{}^j$, or more generally, for the $3 \times 3$ matrix

$$\bar{\delta}^T\bar{\delta} = \sum_{j=1}^{N} \delta^{jT}\delta^j$$

in Eq. (21). This interpretation follows from the consideration of limiting cases. If the appendage is very nearly rigid, the transfer function of Eq. (21) must reduce to the rigid vehicle transfer function $G(s) = 1/(I_\alpha s^2)$. This is assured by the terms $\sigma_j{}^2$ in the denominator of each term in the sum. If, on the other hand, the appendage is extremely flexible in all directions, one must expect the transfer function to be the rigid body transfer function of the base alone, since the appendage is essentially detached as far as response to base oscillations at control frequency is concerned. As all $\sigma_j$ in Eq. (21) approach zero, this equation becomes

$$\theta(s) = \left[ \left( I - \sum_{j=1}^{N} \delta^{jT}\delta^j \right) s^2 \right]^{-1} T(s) \quad (24)$$

Thus the $3 \times 3$ matrix

$$I - \sum_{j=1}^{N} \delta^{jT}\delta^j = I - \bar{\delta}^T\bar{\delta}$$

must be the inertia matrix of the vehicle for the vehicle mass center, less the appendage inertia. This quantity can vary therefore from zero to $I$, and $\mathfrak{R}_\alpha{}^j = 1 - \delta_\alpha{}^j\delta_\alpha{}^j/I_\alpha$ can range from nearly zero for an extremely large appendage, very

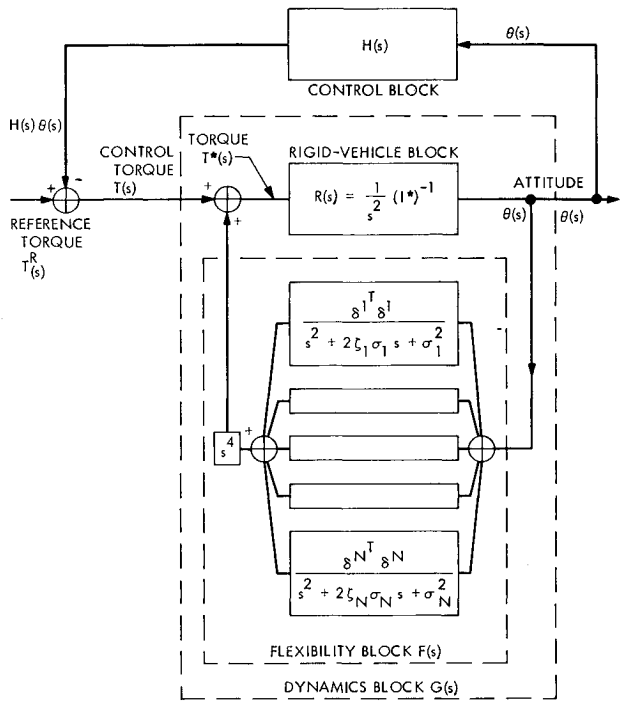


**Fig. 2 Control system block diagram.**

responsive to $\theta_\alpha$ in its $j$th mode, to unity for a small appendage or an appendage not responsive to $\theta_\alpha$ in its $j$th mode.

The single-axis scalar transfer function for the closed loop control system about axis $\alpha$ can be obtained by substituting Eq. (23) in Eq. (22), assuming that $H(s)$ is also a diagonal matrix, and the locus of the roots of the characteristic equation

$$1 + G_\alpha(s)H_\alpha(s) = 0 \quad (25)$$

can then be plotted as some gain parameter which is a factor in $H_\alpha(s)$ varies from zero (locating the poles) to infinity (locating the zeros).

It is instructive to consider in advance of control system design the locations of those poles and zeros produced by the open-loop transfer function $G_\alpha(s)$. To find the open-loop poles, one sets the denominator of $G_\alpha(s)$ to zero and solves for $s$, and the zeros are found similarly from the numerator. When a single mode is retained, as in Eq. (22), these roots become

$$p_1 = p_2 = 0 \quad (26a)$$

$$p_{3,4} = [-\zeta_j \pm i(\mathfrak{R}_\alpha{}^j - \zeta_j{}^2)^{1/2}]\sigma_j/\mathfrak{R}_\alpha{}^j \quad (26b)$$

$$z_{1,2} = \sigma_j[-\zeta_j \pm i(1 - \zeta_j{}^2)^{1/2}] \quad (26c)$$

where $i = (-1)^{1/2}$. Examples of computer-generated root-locus plots for the single-axis response of specific systems appear in subsequent sections.

## Example: An Idealized Test Vehicle

In order that the development of methods of control system design not be obscured by the mechanical complexity of the object being controlled, a simple, idealized test vehicle (Fig. 3) has been devised to permit physically meaningful interpretation of all phases of the analysis. (Later, we apply the same methods to a design for the Thermoelectric Outer Planet Spacecraft, TOPS). Figure 3 shows four elastic members attached to a rigid body $B$ which may also contain a rigid, symmetric rotor. The elastic bodies are massless except for a tip mass on each, normalized to unity (weight 1 lb). The central body $B$ (including its rotor) weighs 4 lb, so the

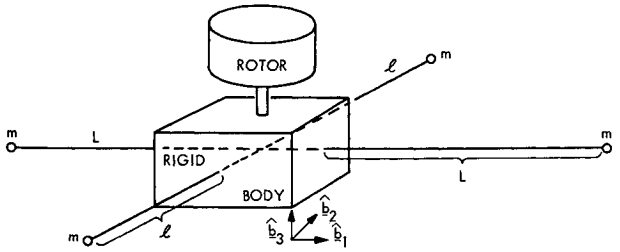


**Fig. 3 Test vehicle.**

vehicle mass is distributed equally between the rigid part and the four flexible attachments, which together comprise what will be called a single appendage. The tip masses are particles, and the central body is inertially spherical, with weight moment of inertia 2590 lb-in.$^2$ and dimensions small relative to beam lengths $L$ and $l$, chosen as 4 ft and 2 ft, respectively. Beam stiffnesses are chosen to make the long beams have natural frequencies of 0.90 and 1.81 Hz, respectively, in the 1-2 and 1-3 planes of the vehicle when attached to a stationary base $B$. The corresponding "cantilever mode" natural frequencies of the short beams are 2.71 and 4.52 Hz in the 1-2 and 2-3 planes, respectively. For the investigations reported in this paper, all beams are assumed longitudinally inextensible.

The modal coordinates in the matrix $\bar{\eta}$ of Eqs. (1) and (2) are not the cantilever modal coordinates of the individual beams, nor are they normal-mode coordinates of the total vehicle. (The presence of the rotor makes the vehicle normal-modes complex, and these modes are not used here in order to confine the analysis to real numbers.) The coordinates in $\bar{\eta}$ establish the response of the appendage in modes in which they would vibrate freely if the rigid body was free in translation but constrained against rotation. With this interpretation, it becomes evident that there must be eight coordinates in the column matrix $\eta$, and for this simple system one can almost guess the mode shapes.

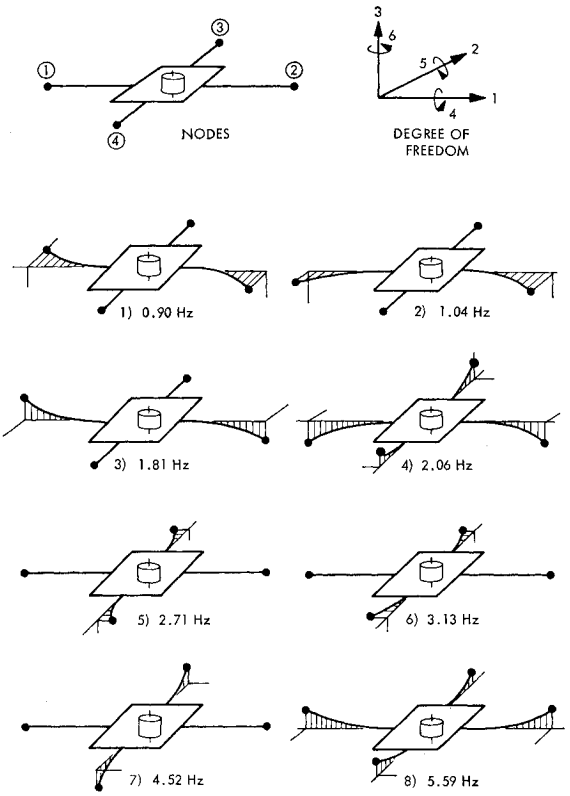


**Fig. 4 Mode shapes for test vehicle.**

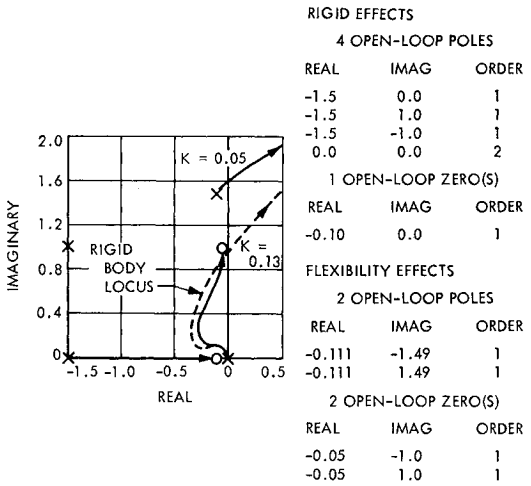


**Fig. 5 Rigid and flexible test vehicles under lead-lag control with complex poles.**

Using established digital computer eigenvalue-eigenvector routines, one can determine the eight natural frequencies and mode shapes quite accurately.‡ Results are presented schematically in Fig. 4, and quantitatively in Table 1. In the latter, node numbers and numbers associated with degree of freedom are to be obtained from the first diagram of Fig. 4.

For purposes of preliminary design, it may be desirable to make exploratory transfer function calculations before the appendage is fully defined and subjected to modal analysis. Examination of the matrix transfer function in Eq. (9) reveals that of the appendage properties only the matrices $\bar{\sigma}$, $\bar{\zeta}$, and $\bar{\delta}$ are required. The autopilot transfer function in Eq. (20) does involve other appendage properties, but in the first approximation Eq. (9) will suffice for autopilot control also. Since $\bar{\zeta}$ is actually assigned and not calculated, only $\bar{\sigma}$ and $\bar{\delta}$ must be calculated for application of the transfer function in Eq. (9).

For this simple system one can readily estimate $\sigma_1 \cong 0.9$ Hz, since this is the input cantilever mode natural frequency of the longest beams. Furthermore, one can utilize the physical interpretation of $\bar{\delta}^T\bar{\delta}$ offered in the previous section, and guess that in the first mode only the long beams will partici-

**Table 1 Mode shapes (M1-M8, see Fig. 4) and frequencies**

| Node/ degree of freedom | Mode | | | | |
|---|---|---|---|---|---|
| | M1 | M2 | M3 | M4 | M8 |
| 1/2 | 0.707 | −0.817 | 0 | 0 | 0 |
| 1/3 | 0 | 0 | 0.707 | −0.799 | 0.335 |
| 1/5 | 0 | 0 | 0.022 | −0.025 | 0.010 |
| 1/6 | −0.022 | 0.026 | 0 | 0 | 0 |
| 2/2 | −0.707 | −0.817 | 0 | 0 | 0 |
| 2/3 | 0 | 0 | −0.707 | −0.799 | 0.335 |
| 2/5 | 0 | 0 | 0.022 | 0.025 | −0.010 |
| 2/6 | −0.022 | −0.026 | 0 | 0 | 0 |
| | M4 | M5 | M6 | M7 | M8 |
| 3/1 | 0 | −0.707 | −0.817 | 0 | 0 |
| 3/3 | 0.050 | 0 | 0 | 0.707 | 0.865 |
| 3/4 | 0.003 | 0 | 0 | 0.044 | 0.054 |
| 3/6 | 0 | 0.044 | 0.051 | 0 | 0 |
| 4/1 | 0 | 0.707 | −0.817 | 0 | 0 |
| 4/3 | 0.050 | 0 | 0 | −0.707 | 0.865 |
| 4/4 | −0.003 | 0 | 0 | 0.044 | −0.054 |
| 4/6 | 0 | 0.044 | −0.051 | 0 | 0 |

‡ Appreciation is expressed to J. Garba of JPL, who actually performed these computer operations, using the SAMIS program.

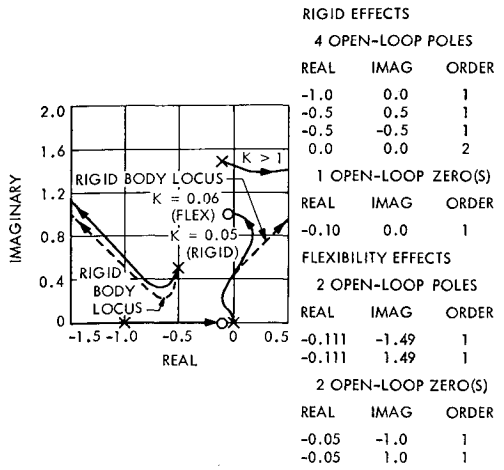


**Fig. 6 Rigid and flexible test vehicles of Fig. 5 with new pole locations.**

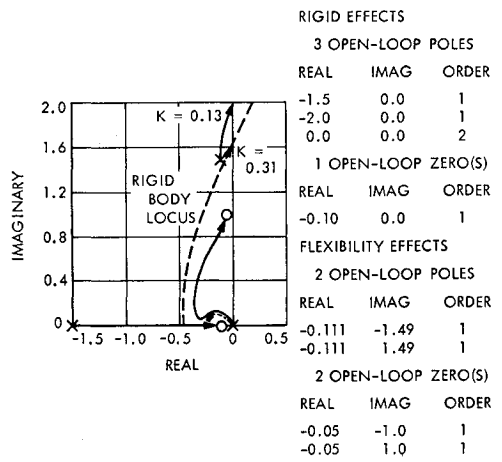


**Fig. 7 Rigid and flexible test vehicles under lead-lag-lag control.**

pate (as in Fig. 4); $\delta_3{}^j\delta_3{}^j$ should therefore be given by 2 (1 lb) (48 in.)$^2 \cong$ 4600 lb-in.$^2$, since this figure represents the contribution to $I_3$ of the two long beams. One might for this simple system easily guess as well the third, fifth, and seventh mode frequencies and contributions to $\bar{\delta}^T\bar{\delta}$, since these are asymmetric modes which have frequencies corresponding to the known cantilever mode frequencies. The physical interpretation of $\bar{\delta}^T\bar{\delta}$ tells us that the symmetric modes (modes 2, 4, 6, and 8 in Fig. 4) contribute nothing to this matrix, so they can be completely ignored.

Confirmation of these estimates for frequencies and $\delta^{iT}\delta^i$ contributions comes from the computer-generated value of $\bar{\delta}$, using the definition following Eq. (2). The results for $\delta$ and $\delta^T\delta$ (with no truncation) are given by

$$\delta = \begin{bmatrix} 0 & 0 & -2a \\ 0 & 0 & 0 \\ 0 & 2a & 0 \\ 0 & 0 & 0 \\ 0 & 0 & a \\ 0 & 0 & 0 \\ a & 0 & 0 \\ 0 & 0 & 0 \end{bmatrix} \qquad \delta^T\delta = \begin{bmatrix} b & 0 & 0 \\ 0 & 4b & 0 \\ 0 & 0 & 5b \end{bmatrix}$$

where $a$ = 33.94 lb-in.$^2$; $b$ = 1150 lb-in.$^2$; and computer generated numbers below $10^{-5}$ have been replaced by zeros. (For unit consistency it must be noted that $\delta^T\delta$ is actually $\delta^T E^{-1}\delta$, with $E$ a unit inertia matrix.) For this simple system, the estimated values are entirely correct. (The predicted $\delta_3{}^1\delta_3{}^1$ = 4600 lb-in.$^2$ checks $-67.88$ squared, and the calculated $\delta^T\delta$ is precisely the contribution of the appendage masses to the vehicle inertia matrix. Furthermore, the even-numbered rows of $\delta$ are null, so these modes do not contribute to $\delta^T\delta$.)

Having obtained, by estimation or calculation, the necessary parameters of the flexible vehicle, the control system designer can begin the sequence of response analyses required for selection of a control system. In general, the first step might be the rapid construction of a number of root-locus plots for single-axis response, the second step might then be a series of eigenvalue studies for a smaller range of preliminary control system designs, and the final step would be a numerical integration of the most general system of equations of motion, to confirm the final control system design. For the simple test vehicle treated in this section, however, each appendage modal vibration contributes to the vehicle response about one axis only, so the three scalar equations of vehicle motion [Eq. (1)] are coupled only by the "gyroscopic coupling" of the rotor. Furthermore, response $\theta_3$ about the $\hat{\mathbf{b}}_3$ axis (see Fig. 3) is completely uncoupled from responses $\theta_1$ and $\theta_2$ about axes $\hat{\mathbf{b}}_1$ and $\hat{\mathbf{b}}_2$, so root locus plots for this axis must indicate precisely the same response that would be obtained from eigenvalue calculations or numerical integrations. The purposes of this paper are best served by restricting the test vehicle analysis results to the presentation of root locus plots for $\theta_3$. In the next section eigenvalue analyses and integration results are presented for a space vehicle of realistic complexity.

Figures 5–8 portray root-locus plots for $\theta_3$ response of the test vehicle, under various assumptions. The dashed-line loci on Figs. 5–7 are based on the assumption that the vehicle is *rigid*, so they provide for three simple control systems a basis for evaluating the influence of flexibility. Figures 5–7 introduce flexibility in the first mode of vibration (see Fig. 4 and Table 1). In this mode the normalized reduced inertia $\mathcal{R}_3{}^1$ is $1 - (\delta_3{}^1\delta_3{}^1/I_3) = 1 - [4600/(2590 + 5750)] = 0.45$. The natural frequency $\sigma_1$ is 0.90 Hz, although in the plots this value is normalized to unity. The damping ratio $\zeta_1$ is assumed to be 0.05 (a relatively high figure is chosen to improve the visual impact of the root locus plot). From Eqs. (26), the poles and zeros of the open-loop transfer function $G_3(s)$ may be obtained. With $\sigma_1$ normalized to unity, these roots become

$$p_{1/2} = 0{,}0, \quad z_{1/2} = -0.05 \pm i, \quad p_{3/4} = -0.111 \pm i\,1.49$$

For Fig. 5 the controller (feedback) transfer function $H_3(s)$ has a pair of complex poles, a real zero and a real pole of larger magnitude (so it might be called a lead-lag system with complex poles). The influence of flexibility on the locus is not surprising, but the "crossover gain" which marks the transition to instability is drastically reduced by the flexible ap-

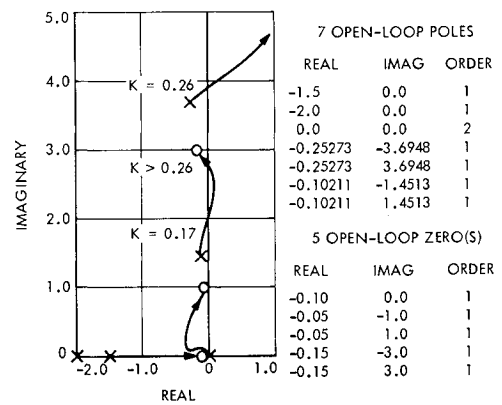


**Fig. 8 Two-mode flexible test vehicle under lead-lag-lag control.**

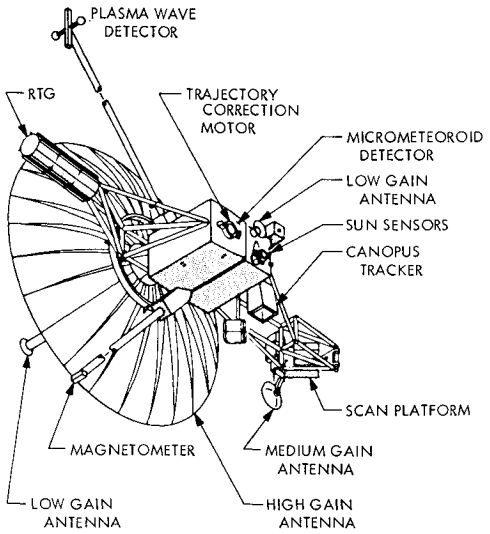


**Fig. 9 Thermoelectric outerplanet spacecraft (TOPS).**

pendage. Whereas a rigid vehicle would become unstable when the gain reaches 0.13, Fig. 5 shows instability to result when the gain becomes 0.05. This is a reduction for the flexible vehicle to 38% of the crossover gain for the rigid vehicle.

Parenthetically, it may be noted that the gain $K$ employed in these root locus plots is related to the gain $K'$ which appears as a factor in the feedback transfer function by a factor which from Eq. (26) is uninfluenced by the flexibility of a single mode. Thus changes in root locus plot gain $K$ due to flexibility can be interpreted directly as changes in the actual feedback controller gain $K'$.

Figure 6 is, like Fig. 5, based on a lead-lag control system with a pair of complex poles. The poles of $H_\alpha(s)$ in Fig. 6 are somewhat closer to the origin than in the previous example. The crossover gain for the flexible vehicle appears to be 20% higher than for the rigid vehicle, whereas this gain is 62% lower when the complex pole of $H_\alpha(s)$ matches the structural frequency, as in Fig. 5. Thus generalizations regarding the influence of appendage flexibility on control system stability would appear to be dangerous, and superficial physical interpretations unwise.

Figure 7 portrays the rigid vehicle response to a "lead-lag-lag" controller, with a negative real zero and two more remote negative poles (one of which is off the plot at $-2.0$). The crossover gain is $K = 0.31$. Figure 7 illustrates the influence of the first mode flexibility of the appendage, which reduces the crossover gain to 0.13, 42% of its original value. Figure 8 indicates the influence of the first and second modes of appendage vibration in combination.

For a "pure gain" direct feedback control, root-locus plots (not shown) can be deduced by inspection. It can be established by use of the Routhian array that such control systems

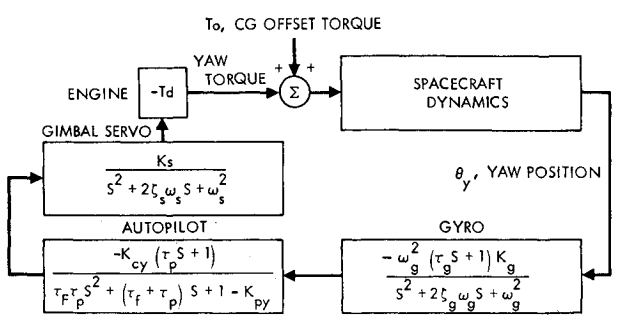


**Fig. 10 Linearized and simplified yaw autopilot loop.**

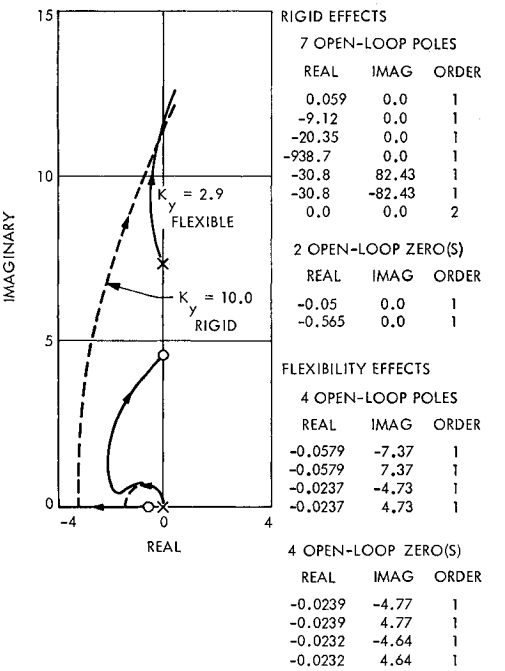


**Fig. 11 TOPS autopilot yaw axis root loci (rigid and flexible vehicles).**

cannot be destabilized by appendage flexibility. (See Ref. 10, pp. 72–74 for details.)

For this idealized test vehicle there were generated 35 root locus plots, of which those preceding are typical. With a standardized program (written by E. H. Kopf and R. Mankovitz), each plot required only 10 to 40 sec of IBM 7094 time, depending on the number of plots requested in a given run. For the single-axis linear response of a vehicle as simple as this vehicle, the conclusions are quantitatively precise. For a vehicle of realistic complexity (as treated in the next section), root locus plots may lose quantitative validity, while preserving the qualitative significance normally sought in preliminary design studies.

## Example: The TOPS Autopilot

The unmanned TOPS is intended to perform scientific investigations of Jupiter, Saturn, Uranus, and Neptune in the late 1970's. Its configuration (Fig. 9) is dominated by a 14-ft-diam parabolic communications antenna and a bank of radioisotope thermoelectric generators (RTGs). In addition, a pair of telescoping booms are required to provide separation for sensitive instruments (magnetometers, plasma wave detector, etc.). Much of the remaining scientific instrumentation has been provided viewing area (around the antenna) and separation from RTG radiation by mounting it on a large foldout structure opposite the RTG foldout boom. Finally, central to the craft is an electronic equipment compartment carrying the autopilot's attitude sensors (high-gain gyros) and actuator (gimbaled engine). It is this portion of the vehicle that will be considered the rigid body to which the flexible appendages (RTG, science, and magnetometer booms; antenna) are attached.

Although the hybrid coordinate formulation is also the ideal approach for the TOPS cruise attitude control system because of the use of momentum wheels, the discussion here is limited to initial investigations of the autopilot which maintains vehicle attitude during the trajectory correction motor's thrusting periods. The gimbaled engine provides attitude control about the pitch and yaw axes, whereas roll control is maintained by the roll gas jets, which, in the cruise control mode, are normally used to desaturate the roll wheels.

**Table 2 TOPS hybrid-coordinate structural model data**

| Mode $i$ | $\sigma_i$, Hz | $\phi^T M \Sigma_{E0}$ slug-ft $x$ | $y$ | $z$ | $\delta$ slug-ft$^2$ $x$ | $y$ | $z$ |
|---|---|---|---|---|---|---|---|
| 1 | 0.74 | 0.6381E-4 | 0.7994E-4 | 0.4092E00 | −0.6989E01 | −0.1150E02 | 0.3856E-2 |
| 2 | 0.75 | 0.3130E00 | 0.3519E00 | −0.1537E-3 | −0.3933E00 | 0.3582E00 | 0.1329E02 |
| 3 | 0.76 | 0.2964E00 | −0.3620E00 | −0.1059E-4 | 0.4072E00 | 0.3357E00 | 0.1254E02 |
| 4 | 0.76 | −0.3970E-4 | −0.4834E-4 | 0.5278E00 | −0.8966E01 | 0.8642E01 | −0.1440E-3 |
| 5 | 1.16 | 0.2777E-1 | 0.1248E-2 | 0.1468E-2 | −0.2132E-1 | 0.1469E-1 | 0.4602E01 |
| 6 | 3.85 | −0.2733E01 | −0.30035E-1 | −0.1554E-2 | 0.1673E00 | 0.6115E00 | −0.2636E02 |
| 7 | 5.02 | 0.4006E00 | 0.4416E-1 | 0.2425E-1 | −0.6592E00 | 0.4022E01 | 0.1107E01 |
| 8 | 5.66 | −0.4516E-2 | −0.2416E-2 | −0.1875E00 | 0.8579E00 | 0.1944E01 | −0.7297E-1 |
| 9 | 5.66 | 0.2074E00 | 0.1776E00 | −0.7461E-2 | −0.1245E00 | 0.2310E00 | 0.2673E01 |
| 10 | 5.69 | −0.1780E-1 | 0.9784E-2 | 0.2416E00 | −0.1100E01 | 0.1477E01 | −0.2134E00 |

$$I = \begin{bmatrix} 1139.0 & -1.69 & -2.04 \\ -1.69 & 347.9 & -25.8 \\ -2.04 & -25.8 & 1264.0 \end{bmatrix} \text{ slug-ft}^2, \ \mathfrak{M} = 38.54 \text{ slugs}$$

Pitch, yaw, and roll momentum wheels are switched out during the trajectory correction phase along with their respective cruise optical sensors. Rate and position sensing is provided in all three axes by high-gain, rate-integrating gyros.

Preliminary efforts have attempted to determine the feasibility of using an autopilot control loop originally designed for a Mars orbital vehicle[12] on TOPS as well. A linearized and simplified version of the proposed autopilot yaw axis (or pitch) loop is shown in Fig. 10. Among the assumptions made to develop the simple, single-axis system model was that gimbaled engine reaction torques on the craft would not be considered, i.e., the engine is assumed massless. Also, as discussed previously, the influence on $\theta$ (pitch or yaw) of constant thrust $F_0$ along the vehicle roll axis is ignored; only the effects of the *torque* applied by the gimbaled motor and the resulting rigid-flexible body interactions are included.

Of course, the three-stage design process to be executed for the TOPS autopilot system must be based on the existence of a detailed hybrid coordinate structural model of the craft pictured in Fig. 9. Such a model was developed§ relatively quickly (2 weeks) using 20 discrete sub-bodies to approximate the flexible members. The result of computer calculations to transform the discretized structural model into hybrid coordinate modal data is summarized, in part, in Table 2. Shown are the first ten modal frequencies obtained and corresponding elements of the matrices $\delta$ and $\phi^T M \Sigma_{E0}$. Approximately 30 modes were available in all from the computer generated data.

It is at this stage that one must begin to weigh the importance of the modes and, tentatively at least, truncate the modal data. The first five modes, grouped near 1 Hz may be traced to the antenna and magnetometer booms. One can see from the size of coefficients in $\delta$ that pitch and yaw axes are predominantly affected by modes 1 and 4 while roll largely sees modes 2, 3, and 5. Based on very simple modeling of the craft as a rigid body hinged to two rigid booms, natural frequencies of vibration above 4 Hz were shown to have little effect on autopilot stability. Therefore modes beyond 5 were removed from the dynamic model for all phases of the analysis including the detailed computer simulation. An additional excuse for deleting the significantly higher frequency modes is the dramatic improvement in numerical integration speed if digital simulation is employed.

Equation (22) can now be of use in examining the linearized, single-axis control loop. For both pitch and yaw, modes 1 and 4 appear to dominate in the $\delta$ matrix, so that $\theta_y$ and $\theta_x$ could be approximated by equations of the form

$$\frac{\theta_y(s)}{T_y(s)} = \left[ I_{yy}s^2 - s^4 \frac{\delta_y{}^1 \delta_y{}^1}{(s^2 + 2\zeta_1\sigma_1 s + \sigma_1{}^2)} - s^4 \frac{\delta_y{}^4 \delta_y{}^4}{(s^2 + 2\zeta_4\sigma_4 s + \sigma_4{}^2)} \right]^{-1}$$

[The equation for $\theta_x(s)/T_x(s)$ is identical in form.] With the substitutions $I_{xx}$, $I_{yy}$, $\delta_y{}^1$, $\delta_x{}^1$, $\delta_y{}^4$, $\delta_x{}^4$ = 1139.0, 347.9,

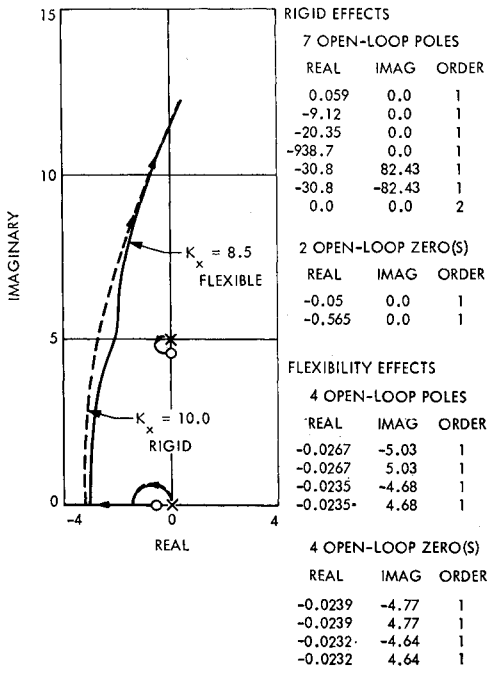


**Fig. 12 TOPS autopilot pitch axis root loci (rigid and flexible vehicles).**

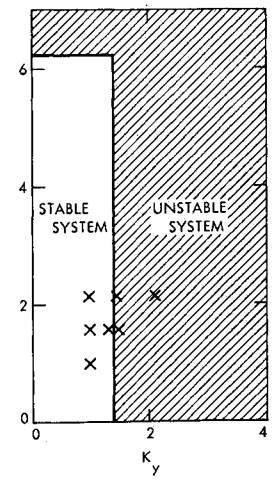


**Fig. 13 Result of eigenvalue analysis ($x$ = point checked by computer simulation).**

§ Thanks must go to R. Bamford and C. Helberg, who modeled the structure and performed the necessary computer calculations.

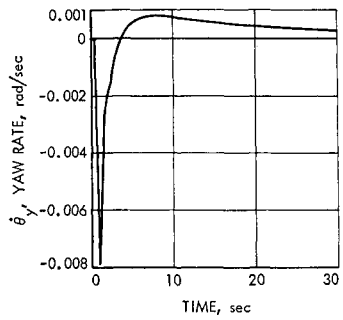


**Fig. 14 TOPS yaw rate vs time, rigid vehicle, $K_{x,y} = 2.2$.**

$-11.5$, $-6.989$, 8.642, and $-8.966$ slug-ft$^2$, respectively, and $\sigma_1$, $\sigma_4$ = 4.65 and 4.76 rad/sec, respectively, and $\zeta_1$, $\zeta_4$ = 0.005, the resulting transfer functions for yaw and pitch are

$$\frac{\theta_y(s)}{T_y(s)} = \frac{(s^2 + 0.0465s + 21.62)(s^2 + 0.0476s + 22.8)}{347.9s^2(0.405s^4 + 0.066s^3 + 31.1s^2 + 2.09s + 493)}$$

$$\frac{\theta_x(s)}{T_x(s)} = \frac{(s^2 + 0.0465s + 21.62)(s^2 + 0.0476s + 22.8)}{1139s^2(0.887s^4 + 0.089s^3 + 41.9s^2 + 2.09s + 493)}$$

The open-loop poles and zeros of the linearized, single-axis autopilot system of Fig. 9 may now be plotted as shown in Figs. 11 and 12. The dashed lines on Figs. 11 and 12 indicate the closed-loop root locations under the ideal, totally rigid spacecraft condition where the control parameters are nominally specified as: $\tau_G$ = 1.77 sec, $\tau_F$ = 0.111 sec, $\zeta_G$ = 0.35, $K_P$ = 2.2, $\omega_G$ = 88.0 rad/sec, $\zeta_s$ = 3.47, $\tau_P$ = 20.0 sec, and $\omega_s$ = 138.2 rad/sec; gimbal servo poles: $-938.66$, $-20.35$; gyro poles: $-30.8 \pm 82.4\ i$; autopilot poles: $-9.12$, $+0.059$; gyro zero: $-0.565$; and path guidance zero: $-0.05$.

Loop gain (d.c. or Bode gain) at the point of marginal stability is 10.0. On the other hand, in Fig. 11 the yaw axis loop with approximated flexible spacecraft dynamics shows a drastically changed root locus with a critical gain reduced to 2.9. While the pitch-axis root locus for the flexible case also departs significantly from the rigid case, critical gain reduction is only to 8.5. The fact that the total pitch axis moment of inertia is about 3.3 times as great as yaw's obviously was responsible for the difference in location of the flexible appendage pole-zero contributions to each axis and the effect on critical loop gain values.

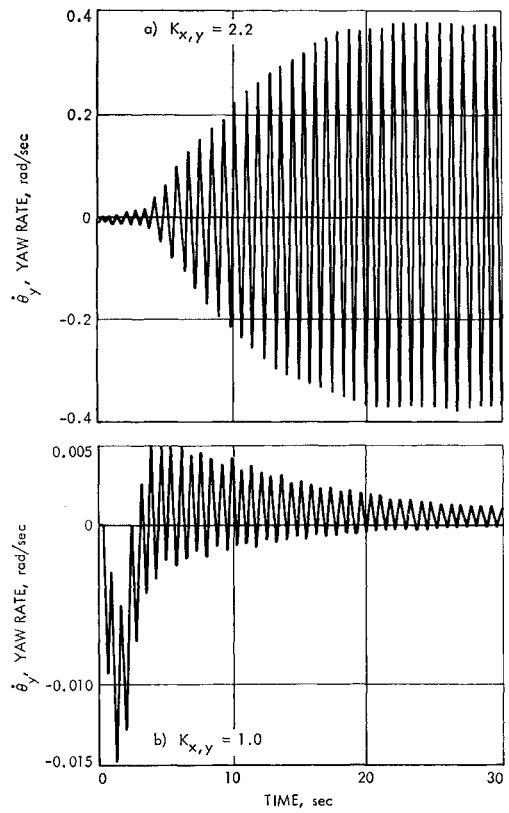


**Fig. 15 TOPS yaw rate vs time, flexible vehicle.**

An examination of the rigid-body autopilot system reveals closed-loop bandwidths of about 0.3 and 0.8 Hz corresponding to d.c. loop gains of 1.0 (0 db) and 3.16 (10 db), respectively. It is clear that the first four appendage modes have already entered the control bandwidth at the latter gain level and, in the case of yaw, caused instability.

One might expect that, if additional modes are used in the initial single-axis root locus analyses, critical gain values would decrease even more. Further, the fact that interaxis coupling might require even more substantial loop gain reductions to maintain stability suggests an eigenvalue analysis of the complete system. The TOPS autopilot may be arranged into state variable form to give a 30 × 30 system state matrix including pitch, yaw, and roll angles, five flexible appendage modes, and the various control dynamics. Figure 13 shows that when the detailed, coupled case is considered, yaw loop stability deteriorates further and essentially controls the stability of the entire system.

A digital simulation was programmed and included nonlinearities due to 1) gimbal servo drive amplifier saturation, 2) the saturation characteristic built into the compensation block to prevent reaching mechanical gimbal stops, and 3) the roll axis bang-bang control loop. (It did not include gimbal actuator stiction.) The level of detail was such as to include effects of gimbal mounting errors and center-of-mass displacements due to appendage deformations, and the hybrid coordinate formulation represented by Eqs. (1) and (2) was implemented in detail. Yaw-axis response is shown for three cases in Figs. 14 and 15 to illustrate the computer simulation results. In each case, the autopilot controller and spacecraft are responding to the engine turn-on transient (100-lb thrust) under the conditions of an initial pitch axis center-of-mass offset of 0.02 ft. Five flexible modes are used in each case in Fig. 15; for gains of 2.2 the flexible vehicle proves to be unstable (Fig. 15a) as the eigenvalue analysis predicted. Reduction of $K_{x,y}$ to 1.0 results in a stable response (Fig. 15b), which also agrees with eigenvalue predictions.

## Conclusions

A three-stage method for the design of attitude control systems for flexible spacecraft, and its use to illustrate the potentially destabilizing influence of appendage flexibility, have been presented. The design procedure employs root-locus plots, eigenvalue analyses, and numerical integrations to permit an efficient convergence on control system design. Root-locus plots are presented for an idealized flexible "test vehicle" subjected to a variety of simple control laws. Although in some cases appendage flexibility has no significant influence on control system design, similar control systems are influenced substantially by flexibility. Gains marking the transition to instability are reduced as a result of flexibility by as much as 62% of the value obtained for the rigid vehicle.

For a vehicle of such complexity as the Thermoelectric Outer Planet Spacecraft (TOPS) root-locus plots provide only qualitatively useful information, while correlation between eigenvalue results and numerical integration remains good. For TOPS, as for the idealized test vehicle, the "crossover gain" to instability was substantially reduced by flexibility. On the basis of root-locus plots, the TOPS crossover gain in yaw was reduced by 71% due to flexibility, and eigenvalues indicate an even larger reduction.

## References

[1] Likins, P. W., and Gale, A. H., "The Analysis of Interactions Between Attitude Control Systems and Flexible Appendages," IAF AD29, 19th International Astronautical Congress, New York, Oct. 13–18, 1968.

[2] Yu, Y. Y., "Stability of Nonlinear Attitude Control System Including Particularly Effect of Large Deflection of Space Vehicles," IAF AT35, 19th International Astronautical Congress, New York, Oct. 13–18, 1968.

[3] Gevarter, W. B., "Basic Relations for Control of Flexible Vehicles," *AIAA Journal*, Vol. 8, No. 4, April 1970, pp. 666–672.

[4] Noll, R. B., Deyst, J. J., Jr., and Spenny, C. H., "A Survey of Structural Flexibility Effects on Spacecraft Control Systems," AIAA Paper 69-116, New York, 1969.

[5] *Effects of Structural Flexibility on Spacecraft Control Systems*, NASA Space Vehicle Design Criteria Document, NASA SP-8016, April 1969.

[6] Hooker, W. W., and Margulies, G., "The Dynamical Attitude Equations for an N-Body Satellite," *Journal of the Astronautical Sciences*, Vol. 12, No. 4, 1965, pp. 123–128.

[7] Roberson, R. E. and Wittenburg, J., "A Dynamical Formalism for an Arbitrary Number of Interconnected Rigid Bodies, with Reference to the Problem of Satellite Attitude Control," *Proceedings of the 3rd International Congress of Automatic Control*, Butterworth, London, 1967.

[8] Fleischer, G. E., "Multi-Rigid-Body Attitude Dynamics Simulation," TR 32-1516, Feb. 15, 1971, Jet Propulsion Lab., Pasadena, Calif.

[9] Russell, W. J., "On the Formulation of Euations of Rotational Motion for an N-Body Spacecraft," Rept. TR-0200(4133)-2, 1969, Aerospace Corp., El Segundo, Calif.

[10] Likins, P. W., "Dynamics and Control of Flexible Space Vehicles," TR 32-1329, Rev. 1, 1970, Jet Propulsion Lab., Pasadena, Calif.

[11] Gale, A. H. and Likins, P. W., "Influence of Flexible Appendages on Dual-Spin Spacecraft Dynamics and Control," *Journal of Spacecraft and Rockets*, Vol. 7, No. 9, Sept. 1970, pp. 1049–1056.

[12] Kopf, E. H., "A Mariner Orbiter Autopilot Design," TR 32-1349, 1969, Jet Propulsion Lab., Pasadena, Calif.


MARCH 1971 J. SPACECRAFT VOL. 8, NO. 3

# Development of a Biowaste Resistojet

CARL R. HALBACH* AND RONALD Y. YOSHIDA†
*The Marquardt Company, Van Nuys, Calif.*

**The 10-mlb-thrust, concentric-tubes resistojet is being developed for use with biowaste propellants. The selection of a suitable material for the thruster heater parts is discussed; platinum-20% iridium is the present choice. Emphasis is placed on the problems of carbon deposition with propellant mixtures containing methane and of carbonyl attack by $CO_2$. The biowaste resistojets have been strengthened to withstand launch vibration and acceleration loads, and the Mark II model has a trumpet-shaped nozzle with an expansion ratio of 400. Thrusting performance for methane, carbon dioxide, water, hydrogen, and typical biowaste propellant mixtures is presented.**

## Introduction

STUDIES of manned space stations show that some waste products (e. g., $CH_4$, $CO_2$, $H_2O$, and $H_2$) from the life support systems will be available for use as rocket propellants for attitude-control and station-keeping propulsion. The biowaste propulsion system becomes part of a mass-conservative attitude-control system utilizing control moment gyros.[1] This paper presents a status report on a program[2] to develop 10-mlb-thrust resistojets for this purpose, using the life-test-proven[3] concentric-tubes resistojet concept shown schematically in Fig. 1. It consists basically of an electric-resistance-heated, 3-pass heat exchanger and a nozzle for accelerating the heated gas. The electrical flow is through the outer case, nozzle, and inner heating elements; 85% of the ohmic heating takes place in the inner heating element. This design offers the following advantages relative to a single-tube-type resistojet: high thermal efficiency for low power consumption, final gas temperature close to maximum wall temperature for high specific impulse, minimized creep stresses with zero hoop-creep stress in the hottest inner element for long life, and a higher-voltage, lower-current power characteristic, which is desirable. The biopropellants can include mixtures which range through oxidizing, reducing and carburizing atmospheres. Thruster design changes relative to the life-tested thruster include heater material and adaptation of the structure for launch vibration-acceleration load handling capability.

Recieved August 18, 1970; presented as Paper 70-1133 at the AIAA 8th Electric Propulsion Conference, Stanford, Calif., August 31–September 2,1970; revision received November 16, 1970. Work supported by NASA Langley Contract NAS1-9474.

* Senior Project Engineer, Propulsion Division. Member AIAA.

† Program Manager, Propulsion Division. Member AIAA.

## Heater Material Selection

The concentric-tubes resistojet in the thin-walled, high-efficiency configuration requires the use of ductile metal heater elements. The structural geometry in this design concept is not compatible with the brittleness and poor shock

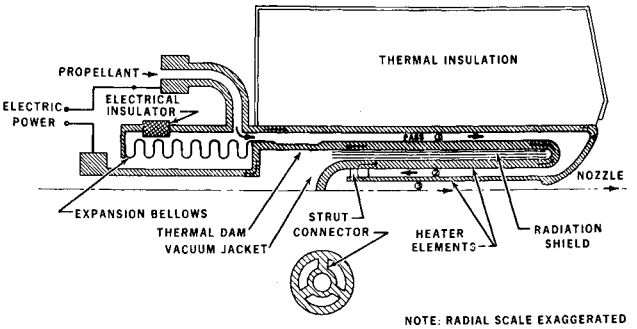


**Fig. 1 Evacuated concentric-tubes resistojet concept.**